Supplementary Online Material of Landau-Zener without a Qubit: Multiphoton Sidebands Interaction and Signatures of Dissipative Quantum Chaos

Léo Peyruchat,[1, 2] Fabrizio Minganti,[2, 3] Marco Scigliuzzo,[2, 4] Filippo Ferrari,[2, 3]
Vincent Jouanny,[1, 2] Franco Nori,[5, 6, 7] Vincenzo Savona,[2, 3] and Pasquale Scarlino[1, 2, *]
[1] *Hybrid Quantum Circuits Laboratory (HQC), Institute of Physics,*
École Polytechnique Fédérale de Lausanne (EPFL), 1015 Lausanne, Switzerland
[2] *Center for Quantum Science and Engineering,*
École Polytechnique Fédérale de Lausanne (EPFL), CH-1015 Lausanne, Switzerland
[3] *Laboratory of Theoretical Physics of Nanosystems (LTPN), Institute of Physics,*
École Polytechnique Fédérale de Lausanne (EPFL), 1015 Lausanne, Switzerland
[4] *Laboratory of Photonics and Quantum Measurements (LPQM),*
Institute of Physics, EPFL, CH-1015 Lausanne, Switzerland
[5] *Theoretical Quantum Physics Laboratory, Cluster for Pioneering Research, RIKEN, Wako-shi, Saitama 351-0198, Japan*
[6] *Quantum Information Physics Theory Research Team,*
Quantum Computing Center, RIKEN, Wakoshi, Saitama, 351-0198, Japan
[7] *Physics Department, The University of Michigan, Ann Arbor, Michigan 48109-1040, USA*

I Construction and solution of the Floquet-Liouvillian problem

The periodically modulated systems described by Eq. (2) in the main text can be described using a stroboscopic Lindblad master equation of period T. The equation of motion of such a system is

$$\hbar \partial_t \hat{\rho}(t) = \mathcal{L}(t)\hat{\rho}(t), \quad \mathcal{L}(t+T) = \mathcal{L}(t). \tag{1}$$

While the temporal dependence of $\mathcal{L}(t)$ prevents the emergence of a true steady state, one can still reach a *stroboscopic* stationary regime.

A The average Floquet steady-state

We are interested in the average properties of the system along one modulation period $T = 2\pi/\Omega$ after a time long enough for the system to have reached a stroboscopic stationary regime. To solve this problem, we assume that, for a long enough time,

$$\hat{\rho}(t) = \sum_{m=-\infty}^{+\infty} \hat{\rho}_m e^{im\Omega t}. \tag{2}$$

One can easily verify that

$$\frac{1}{T}\int_t^{t+T} \hat{\rho}(\tau)\mathrm{d}\tau = \hat{\rho}_0. \tag{3}$$

At this point, one has to determine $\hat{\rho}_0$. A convenient way to find it is to solve it through Fourier analysis (see, e.g., [1, 2]).

The equation of motion can be recast as

$$\begin{aligned} \hbar\frac{\mathrm{d}}{\mathrm{d}t}\hat{\rho}(t) &= \sum_{m=-\infty}^{+\infty} im\Omega\hat{\rho}_m e^{im\Omega t} \\ &= \left[\mathcal{L}_0 + \mathcal{L}_1 e^{i\Omega t} + \mathcal{L}_{-1}e^{-i\Omega t}\right]\hat{\rho}(t) \\ &= \sum_{m=-\infty}^{+\infty}\left[\mathcal{L}_0 + \mathcal{L}_1 e^{i\Omega t} + \mathcal{L}_{-1}e^{-i\Omega t}\right]\hat{\rho}_m e^{im\Omega t}, \end{aligned} \tag{4}$$

where $\mathcal{L}_0$ is the time-independent part of the Liouvillian in Eq. (2) of the main text (i.e., $\zeta = 0$), while $\mathcal{L}_1$ and $\mathcal{L}_{-1}$ represent the decomposition of the modulation. Collecting each term evolving with Ω we have

$$\sum_{m=-\infty}^{+\infty}\left[\left(\mathcal{L}_0 - im\Omega\right)\hat{\rho}_m + \mathcal{L}_1\hat{\rho}_{m-1} + \mathcal{L}_{-1}\hat{\rho}_{m+1}\right]e^{i\Omega t} = 0. \tag{5}$$

If we now assume that each term of the sum is stationary, we obtain the recursion relation

$$\left(\mathcal{L}_0 - im\Omega\right)\hat{\rho}_m + \mathcal{L}_1\hat{\rho}_{m-1} + \mathcal{L}_{-1}\hat{\rho}_{m+1} = 0. \tag{6}$$

By truncating this recursion (i.e., assuming $\hat{\rho}_m = 0$ if $m > M$ or $m < -M$), the problem can be then self-consistently solved.

B Analysis of the Floquet Liouvillian spectrum

A different approach to solving the Floquet problem consists of constructing the so-called *Floquet evolution superoperator* (a Floquet map for Lindbladian systems). Indeed, using the time ordering $\mathcal{T}$, we can formally solve Eq. (1) as

$$\hat{\rho}(t) = \mathcal{T}\left[\exp\left(\int_0^t \mathcal{L}(t')dt'/\hbar\right)\right]\hat{\rho}(0) = \mathcal{F}(t,0)\hat{\rho}(0). \tag{7}$$

$\mathcal{F}(t, t_0)$ is the evolution superoperator for the time-dependent Lindblad master equation. We can then formally introduce the Floquet Liouvillian $\mathcal{L}_{\mathrm{F}}$ as

$$\mathcal{F}(T,0) = \exp\left(\mathcal{L}_{\mathrm{F}}T/\hbar\right). \tag{8}$$

---

[*] E-mail: pasquale.scarlino@epfl.ch

The stroboscopic steady state is the state such that

$$\mathcal{L}_{\rm F}\hat{\rho}_{\rm ss}^{\rm F}=0, \quad \text{or} \quad \mathcal{F}\hat{\rho}_{\rm ss}^{\rm F}=\hat{\rho}_{\rm ss}^{\rm F}. \tag{9}$$

To construct $\mathcal{F}(T,0)$ [3], let us consider

$$\mathcal{F}(T,0)\hat{\rho}_{i,j}, \quad \hat{\rho}_{i,j}=|i\rangle\langle j|. \tag{10}$$

Since $\hat{\rho}_{i,j}$ are an orthonormal basis of the operators space (i.e., any operator can be written as a linear combination of $\hat{\rho}_{i,j}$), we conclude that the matrix form of $\mathcal{F}(T,0)$ can be obtained as

$$\mathcal{F}_{[m=i\cdot(N+1)+j,:]}=\text{vec}\left[\hat{\rho}_{i,j}(T)\right], \tag{11}$$

where $\mathcal{F}_{[m,:]}$ indicates the mth row of the evolution operator in its matrix form, and vec $[\hat{\rho}_{i,j}(T)]$ is the vectorized form of the initial density matrix $\hat{\rho}_{i,j}$ evolved for a time T.

II SQUID arrays as frequency-tunable Kerr resonators

An array of N SQUIDs results in N nonlinear bosonic modes whose dispersion relation can be obtained numerically from the linearized Lagrangian of an effective lumped LC model [4]. The dispersion is linear for the lower frequency modes, and saturates at a high-frequency cutoff close to the plasma frequency of the junctions. Introducing the lowest order nonlinear terms as a perturbation to the previous linear model yields the self- and cross-Kerr terms of each mode [5]. This approximation is valid if the mode frequency ω_i is much smaller than the Josephson energy $E_J/\hbar$ of individual junctions. Increasing the number of SQUIDs in the array reduces both the frequency of the lower modes and the nonlinearity of all modes. The scaling of the frequency and nonlinearities depends on the circuit parameters and the boundary conditions.

The SQUID arrays considered in this work have between $N=10$ and $N=32$ SQUIDs with nominally identical Josephson junctions. One end of the array is shorted to ground, while the other end of the array is left open with a capacitance to ground and to a readout waveguide. Throughout this study we only use the fundamental mode of the SQUID arrays. The frequency of the second mode of the array is approximately twice that of the first mode. Consequently, we can safely neglect the second mode, along with all higher modes of the array. The Josephson inductance of all junctions in the array can be tuned with an external magnetic flux, and the frequency of the first mode the array follows approximately

$$\omega(\Phi_x)=\omega_c\sqrt{|\cos\left(\pi\Phi_x/\Phi_0\right)|}, \tag{12}$$

with ω_c the zero-flux frequency, Φ_x the flux threading the SQUIDs loop and $\Phi_0=h/2e$ the magnetic flux quantum. For the large ratio E_J/E_C of the SQUID's junctions, the Kerr nonlinearity depends weakly on the flux Φ. For the two devices presented here, we choose the flux operating point $\Phi_{\rm wp}$ such that the frequency of the first mode of the arrays is similar, with $\omega_{\rm wp}/2\pi=4.5$ GHz (4.3 GHz) for the $N=10$ ($N=32$) device.

Retaining only the first mode of the SQUID array, and keeping only the first-order nonlinearity, we arrive at the Kerr resonator Hamiltonian in the lab frame,

$$\mathcal{H}/\hbar=\omega_{\rm wp}\hat{a}^\dagger\hat{a}+\chi\hat{a}^\dagger\hat{a}^\dagger\hat{a}\hat{a}\,, \tag{13}$$

with χ the Kerr nonlinearity. After adding a drive $F(\hat{a}e^{-i\omega_d t}+\hat{a}^\dagger e^{i\omega_d t})$ and a frequency modulation $\zeta\cos(\Omega t)\hat{a}^\dagger\hat{a}$, and moving to a frame rotating at the pump frequency ω_d, we obtain the Hamiltonian of Eq. (1) in the main text. We note that to accurately model the Kerr multiphoton resonances of the $N=10$ device, we had to include a higher-order nonlinearity [6].

III Derivation of an effective model for the study of the nonlinear modulated resonators

To simplify the equation of motion Eq. (2) from the main text, we want to eliminate the frequency modulation. To do this, we use the interaction picture $\hat{\tilde{\rho}}(t)=\hat{U}^\dagger(t)\hat{\rho}\hat{U}(t)$, where

$$\begin{aligned}\hat{U}(t)&=\mathcal{T}\exp\left[\int_0^t -i\,dt'\,\zeta\cos(\Omega\,t')\hat{a}^\dagger\hat{a}\right]\\&=\exp\left[-i\frac{\zeta}{\Omega}\sin(\Omega\,t)\,\hat{a}^\dagger\hat{a}\right].\end{aligned} \tag{14}$$

We obtain

$$\hbar\partial_t\hat{\tilde{\rho}}(t)=-i[\hat{\tilde{H}},\hat{\tilde{\rho}}(t)]+\kappa\mathcal{D}\hat{a}\hat{\tilde{\rho}}(t)+\kappa_\phi\mathcal{D}\hat{a}^\dagger\hat{a}\hat{\tilde{\rho}}(t)\,, \tag{15}$$

where

$$\begin{aligned}\hat{\tilde{H}}/\hbar=&\Delta\hat{a}^\dagger\hat{a}+\chi\hat{a}^\dagger\hat{a}^\dagger\hat{a}\hat{a}\\&+F\left\{\hat{a}\exp\left[-i\frac{\zeta}{\Omega}\sin(\Omega\,t)\right]+\text{h.c.}\right\}.\end{aligned} \tag{16}$$

Equations (15) and (16) can be straightforwardly derived thanks to

$$\hat{U}^\dagger(t)\,\hat{a}\,\hat{U}(t)=\hat{a}\exp\left[-i\frac{\zeta}{\Omega}\sin(\Omega\,t)\right]. \tag{17}$$

We finally use the Jacobi-Anger expansion, reading

$$e^{iz\sin\theta}\equiv\sum_{m=-\infty}^{\infty}J_m(z)\,e^{im\theta}\,, \tag{18}$$

where $J_m(z)$ is the mth Bessel function of the first kind, to obtain (up to a phase)

$$\begin{aligned}\hat{\tilde{H}}/\hbar=&\Delta\hat{a}^\dagger\hat{a}+\chi\hat{a}^\dagger\hat{a}^\dagger\hat{a}\hat{a}\\&+\sum_{m=-\infty}^{\infty}F J_m\left(\frac{\zeta}{\Omega}\right)\left[\hat{a}e^{-im\Omega t}+\hat{a}^\dagger e^{im\Omega t}\right].\end{aligned} \tag{19}$$

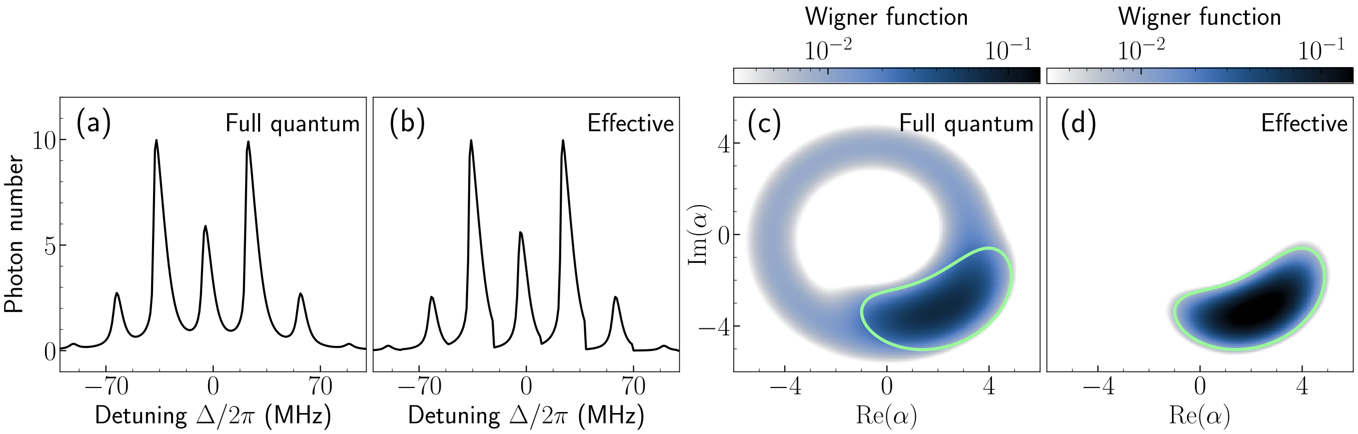

FIG. 1. Comparison between the full Floquet analysis and the effective model derived in Appendix III. We show the photon number n computed with the Floquet steady state [panel (a)] and with the effective Hamiltonian Eq. (3) of the main text [panel (b)]. The full quantum solution and the effective model exhibit a good agreement. We plot in panels (c) and (d) the Wigner function $W(\alpha) = 2/\pi \cdot \mathrm{Tr}\left[\hat{D}_\alpha e^{i\pi\hat{a}^\dagger\hat{a}}\hat{D}_\alpha^\dagger\hat{\rho}\right]$, with $\hat{D}_\alpha = \exp(\alpha\hat{a}^\dagger - \alpha^*\hat{a})$, of the Floquet steady state and the effective model respectively. The green lines in panels (c) and (d) encircles the region where $W(\alpha) > 7\times10^{-3}$ according to the effective model. We conclude that the effective model is reliable when computing $\langle\hat{a}^\dagger\hat{a}\rangle$, i.e., the distance from the center of the distribution $W(\alpha)$. On the contrary, $\langle\hat{a}\rangle$ can not be captured by the simple treatment presented in Appendix III, as evident from the different angular distribution of $W(\alpha)$ obtained from the full and effective model. All physical parameters as in Fig. (6) (d) of main text. We set $\zeta/\Omega \approx 1.67$ and $\Delta/\Omega = -1.1$.

Notice that both dissipation and Kerr nonlinearity remain unchanged by this set of transformations.

Up to this point, no approximations have been made. For the small-drive amplitudes considered in Fig. 3 of the main text, however, we can assume that only one of the driving frequencies is relevant, and discard the fast-rotating terms. Namely, we select only those frequencies around which $\Delta_{\bar{m}} = \Delta - \bar{m}\Omega \simeq 0$, finally obtaining Eq. (3) of the main text.

In Fig. 1 we benchmark the validity of the effective Hamiltonian given by Eq. (2) of the main text for the $N = 32$ device in the Duffing regime at intermediate input power. All the physical parameters have been chosen as in Fig. 6 (d) of the main text. We compare the photon number n computed with the Floquet steady state [Fig. 1 (a)] and with the effective model [Fig. 1 (b)] showing that the two approaches exhibit a good agreement. While the approximation is remarkably predictive in determining the photon number, this is not the case for the coherence $\langle\hat{a}\rangle$. In Figs. 1 (c-d) we compute the Wigner functions obtained from the full quantum simulation of the Floquet steady state and that obtained according to the effective model. While the effective model nicely reproduces the radial distribution of the Wigner function (and thus the photon number), it completely misses the phase, which remains accessible only within the full Floquet-Lindbald treatment described in Appendix I A. In both Figs. 1 (c) and (d) we report the contour of the effective Wigner function, showing that $W(\alpha)$ of the full quantum model contains the effective Wigner function, but the phase coherence is reduced with respect to the effective model. We argue that these dephasing-like effects are due to higher-order processes not accounted for in the effective model, emerging from the combination of Hamiltonian and dissipative terms, and treating them would require higher-order time-dependent perturbation theories such as the Floquet-Magnus expansion.

IV Device characterization

The flux-dependence of the SQUID array frequency is reported for both devices in Fig. 2. The value of the flux Φ_X is controlled by applying a direct current to the external coil. We convert the current applied to the flux threading the SQUIDs by fitting a larger flux modulation sweep over more than one period. The two devices are made of SQUIDs with identical junctions and have a similar total capacitance. As a consequence their maximum frequency differs due to the total number of SQUID N in the two arrays.

We observe an unexplained dip in the flux modulation of device $N = 32$ (blue). This feature is periodically repeated for Φ_0 increments of the flux Φ_X, and we observe no hysteretic effect. This spurious dip was observed across several cooldowns at the same position. A similar device with $N = 46$ SQUIDs located on the same chip does not show a similar dip. Cross markers in Fig. 2 indicate the flux operating point of both devices, and the segment on the x-axes show the maximum flux modulation performed in this work. The $N = 32$ SQUID array is always operated far from the unexpected feature which thus does not impact the results of the experiment.

Because of the nonlinear flux dependence of the frequency of the resonators, the applied frequency modula-

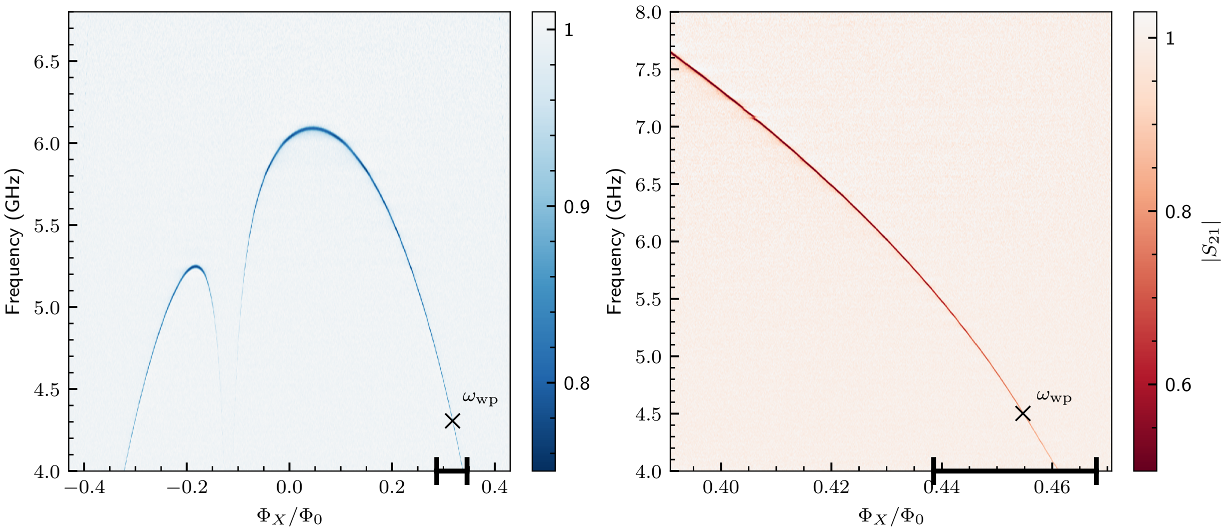

FIG. 2. Measurement of the magnitude of the transmission $|S_{21}|$ as a function of the flux Φ_X in the SQUID arrays for the $N=32$ Duffing device (left, blue) and the $N=10$ Kerr device (right, red). The flux working points used throughout the paper are indicated by cross markers. The black horizontal segments approximately denote the maximum flux modulation reported is in this work with respectively ±0.4 GHz and ±1.0 GHz for the Duffing and Kerr devices.

tion is not exactly sinusoidal, $\zeta\cos(\Omega t)$, as stated in the Hamiltonian Eq. (1) of the main text. Instead, we apply a sinuoisidal modulation of the flux threading the SQUID loop as

$$\Phi_x(t) = \Phi_x^0 + A\cos(\Omega t), \tag{20}$$

with Φ_x^0 the static flux, Ω the frequency of the modulation and A the amplitude of the modulation in Φ_0 unit. Following Eq. 12, the exact frequency modulation is thus given by

$$\omega(\Phi_x(t)) = \omega_c\sqrt{|\cos\left[\pi(\Phi_x^0 + A\cos(\Omega t))/\Phi_0\right]|}. \tag{21}$$

Consequently, for large modulation strength ζ, the frequency modulation is not symmetric around the value without modulation $\omega(\Phi_x^0) = \omega_{\rm wp}$. This results in a deviation of the LZSM resonances $\bar{m}$ away from $\Delta_{\bar{m}}$. We observe this deviation in our measurements, most clearly in Fig. 4 where ζ is as large as 1.0 GHz. It is also apparent in Fig. 6 (d-f) of the main text where the data are systematically shifted to negative frequencies compared to the superimposed numerical simulations. The deviation from the LZ mode position expected for an ideal modulation is towards negative detuning because of the curvature of the flux dependence of the frequency. The deviation increases when the flux operating point is brought closer to zero flux where the curvature is more important. This phenomenon is reported and explained in Ref. [7].

From the measurement of the room-temperature normal-state resistance, we estimate the single junction Josephson energy to $E_J/h \approx 170\,$GHz. The frequencies and Kerr non-linearities of the SQUID array modes can be simulated using a lumped-model and assuming $E_J \gg E_C$ [5]. From this model, we estimate the plasma frequency of the junctions to $\hbar\omega_P = \sqrt{8E_JE_C} \approx h\times 39\,$GHz. The zero-flux frequency of the Kerr $N=10$ device is out of our measurement bandwidth of 4-8 GHz, but we estimate it to be approximately 13 GHz from the lumped model discussed above. We find a single junction charging energy $E_C = e^2/2C_J \approx h\times 1.1\,$GHz. Even for the flux operating point $\Phi_X/\Phi_0 \approx 0.455$ of the $N=10$ device, the effective Josephson energy of the SQUID remains much larger than the charging energy, ensuring the validity of the Kerr approximation of the Josephson Hamiltonian.

V Additional experimental data

In this section, we report additional measurements performed with the $N=32$ Duffing device in the linear regime. In Fig. 3 we repeat the linear regime LZSM interferometry measurements of Fig. 3 (d-f) of the main text for different values of Ω and ζ. The drive power is set to the same low value to remain in the linear regime with a low photon occupation number. In panels (a-d), we sweep the modulation strength ζ for increasing values of modulation frequency Ω. LZSM resonances are visible for $\zeta \geq |\Delta|$, irrespective of the value of Ω. As expected from Eq. (3), the spacing between LZSM resonances is equal to Ω. In panels (e-h), we sweep the modulation frequency Ω for increasing modulation strengths ζ. We observe more and more LZSM resonances as ζ is increased, and again the extension of the resonances is approximately confined to $|\Delta| < \zeta$. These measurements highlight the superb control offered by the platform on the position and number of modes, as for instance in panel (a) we observe clearly LZSM resonances up to mode $\bar{m} = 25$.

Next, in Fig. 4 we repeat the Duffing regime LZSM interferometry of Fig. 6 of the main text, but this time sweeping the modulation frequency Ω at fixed ζ. We re-

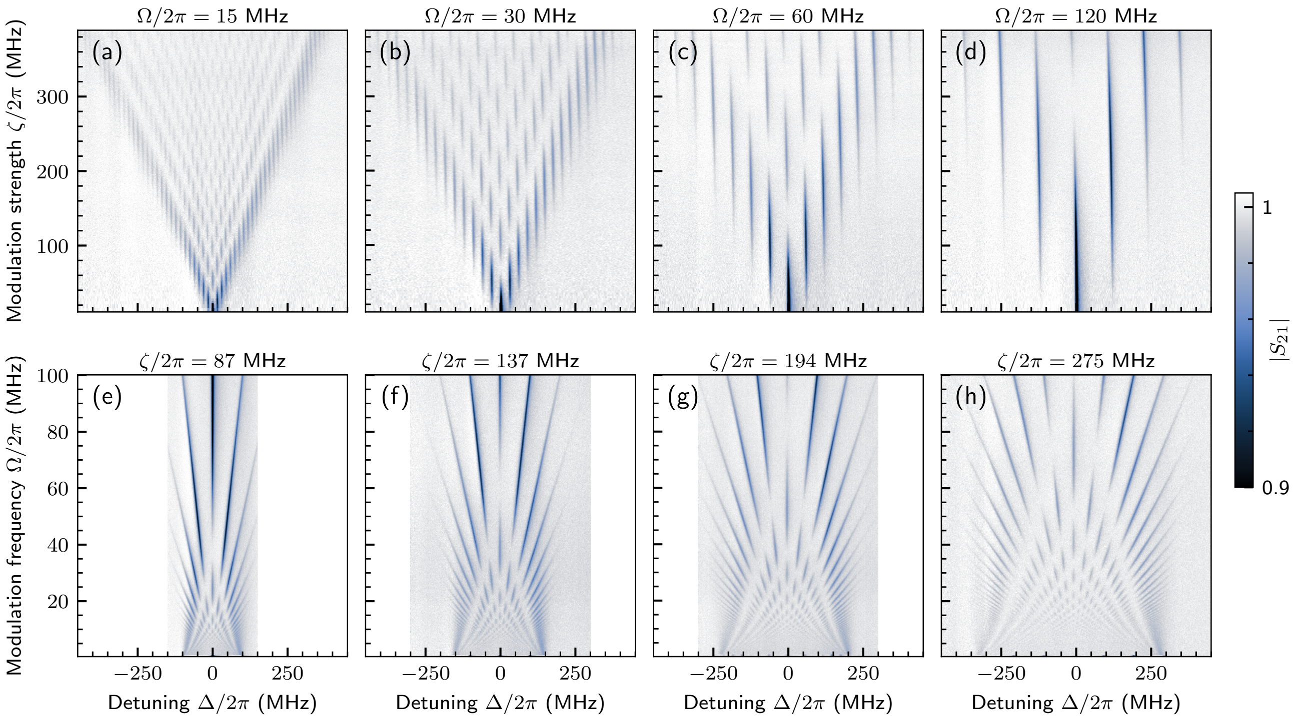

FIG. 3. Extended data of LZSM interference patterns in the linear regime. The measurements are performed on the device N = 32 with the same weak drive power as in Fig. 3 (d-f) of the main text. In panels (a-d), the same sweep of modulation strength ζ is repeated for increasing modulation frequencies Ω. In panels (e-h), the same sweep of modulation frequency Ω is repeated for increasing modulation strengths ζ. These measurements highlight the exquisite control over both the frequency spacing and the number of resonances offered by the platform, with for instance LZSM resonances up to $m = \pm 25$ visible in (a).

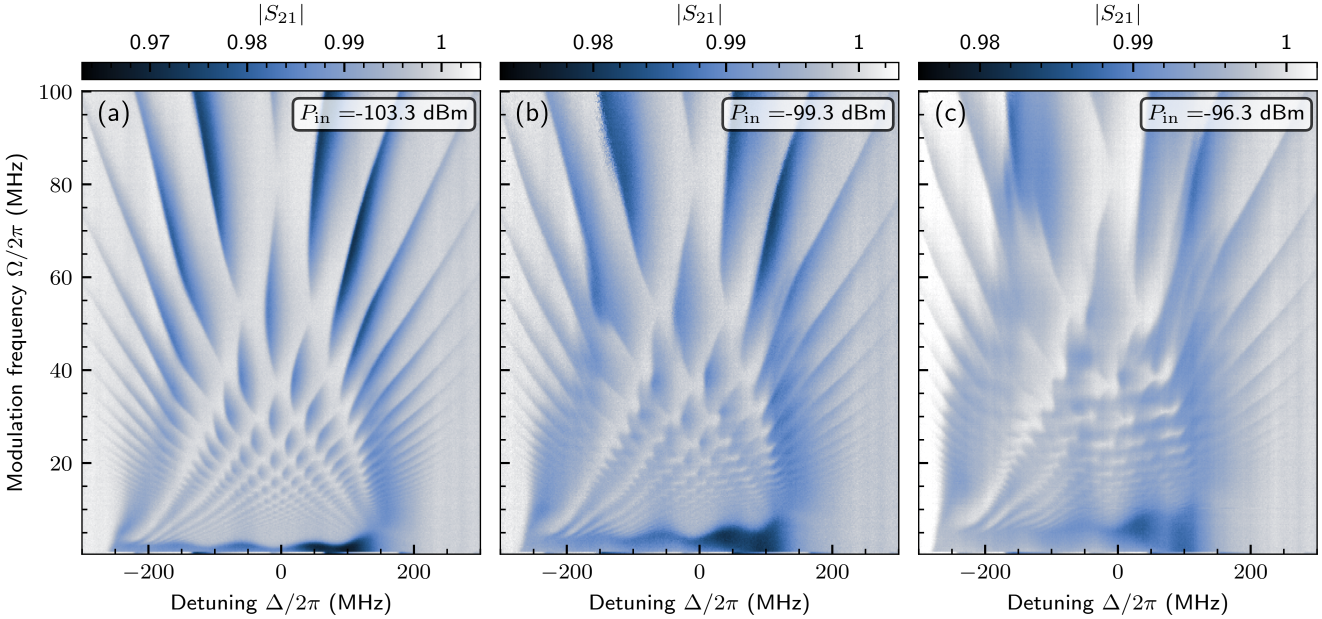

FIG. 4. Extended data of LZSM interferometry in the Duffing regime measured with the $N = 32$ device. The magnitude of S_{21} is measured versus Δ and Ω for increasing drive power P_{in}. The modulation strength is fixed to $\zeta/2\pi = 206$ MHz.

peat this measurement for three increasing values of drive power P_{in}. For the lowest drive shown in panel (a), individual LZSM resonances remain mostly isolated. However, when compared to the linear regime of weak drive, LZSM resonances appear distorted with a rounded shape. This rounding is a combination of the Kerr nonlinearity bending the peak to negative frequencies, and the modulation of the effective drives $F_{\bar{m}}$ that controls the peak bendings. For increasing drive power, as shown in panels (b) and (c), the interference pattern gets more distorted and individual resonances start merging together. In this regime, the effective model of Eq. (3) is no longer valid and a full Floquet-Lindblad treatment is required. As we have theoretically shown, the broadening and distortion of the LZSM interference pattern in the Duffing regime is associated to a dissipative quantum chaotic phase.

---

[1] M. Maragkou, C. Sánchez-Muñoz, S. Lazić, E. Chernysheva, H. P. van der Meulen, A. González-Tudela, C. Tejedor, L. J. Martínez, I. Prieto, P. A. Postigo, and J. M. Calleja, "Bichromatic dressing of a quantum dot detected by a remote second quantum dot," Phys. Rev. B **88**, 075309 (2013).

[2] Vincenzo Macrì, Alberto Mercurio, Franco Nori, Salvatore Savasta, and Carlos Sánchez Muñoz, "Spontaneous scattering of raman photons from cavity-qed systems in the ultrastrong coupling regime," Phys. Rev. Lett. **129**, 273602 (2022).

[3] Fabrizio Minganti and Dolf Huybrechts, "Arnoldi-lindblad time evolution: Faster-than-the-clock algorithm for the spectrum of time-independent and floquet open quantum systems," Quantum **6**, 649 (2022).

[4] Nicholas A. Masluk, Ioan M. Pop, Archana Kamal, Zlatko K. Minev, and Michel H. Devoret, "Microwave Characterization of Josephson Junction Arrays: Implementing a Low Loss Superinductance," Physical Review Letters **109**, 137002 (2012).

[5] T. Weißl, B. Küng, E. Dumur, A. K. Feofanov, I. Matei, C. Naud, O. Buisson, F. W. J. Hekking, and W. Guichard, "Kerr coefficients of plasma resonances in Josephson junction chains," Physical Review B **92**, 104508 (2015).

[6] The resonator exhibits deviation from the pure Kerr nonlinearity prediction due to non-negligible effects of higher nonlinearities, e.g., terms of the form $\chi^{(5)}(\hat{a}^\dagger)^3\hat{a}^3$. We estimate $\chi^{(5)}/2\pi \approx -1.1\,\mathrm{MHz} \simeq 5\%\chi/2\pi$. As such, although the $\chi^{(5)}$ term produces small changes compared to the model in Eq. (1) of the main text, all the relevant physical features of the LZSM interference are captured by the Kerr model. We also note additional nonlinear effects due to the large values of flux modulation used to obtain the wanted ζ.

[7] Tong Wu, Yuxuan Zhou, Yuan Xu, Song Liu, and Jian Li, "Landau–Zener–Stückelberg Interference in Nonlinear Regime," Chinese Physics Letters **36**, 124204 (2019).